A Study of Comb Beam Transmission on Phased Array Weather Radars

Eiichi Yoshikawa, Tomoo Ushio, *Life Fellow, IEEE*, and Hiroshi Kikuchi, *Member, IEEE*

***Abstract*— The comb beam transmission (TX) approach, which forms a power antenna radiation pattern with multiple mainlobes, was studied for application to phased array weather radars. Combining the use of comb TX and a digital beamforming receiver enables a weather radar to observe multiple directions simultaneously. Numerical simulations show that the two-way antenna radiation patterns formed by comb TXs have properties comparable to conventional weather radar observation: almost the same mainlobe widths are achieved, and with reference to the mainlobe peak, the maximum sidelobe level is less than −37 dB, and the sidelobe level reaches −60 dB at an angle of 13.77°. These properties are superior to the wide TXs that are normally utilized by phased array weather radars. A simulation that applied the comb TX approach to a current C-band weather radar showed that the volume scan time can be reduced from almost 500 s to 1 min.**

***Index Terms*— C-band frequency, phased array radar, weather observation.**

I. Introduction

WEATHER radars are currently operating as standard infrastructure in most urbanized areas. Compared with on-site instruments for measuring precipitation, such as rain gauges and disdrometers, weather radars can make observations over wider areas in shorter times. The observation capabilities of weather radars make them indispensable for detecting and warning of hazardous weather phenomena to reduce physical damage and mitigate their impact on social activities. Their capabilities are also crucial for weather prediction. Conventional weather radars have typically operated at S- or C-band frequencies with observation ranges of hundreds of kilometers [1], [2], but the use of X-band weather radars with coverages of tens or 100 km has been growing. The coverage area of an S- or C-band radar can be filled by deploying multiple X-band weather radars in a so-called X-band weather radar network [3]. This gives some new observation capabilities [4]–[7], [8], [9]. These weather radars are able to produce in approximately 10 min a volume scan that contains observations at all azimuth angles and a few tens of elevation angles. This allows detailed observations of hazardous weather phenomena with horizontal extents of more than a few tens of kilometers and lifetimes of a few hours, such as mesocyclones and typhoons [10].

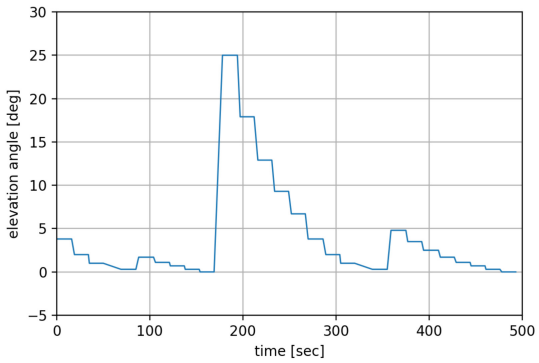

Fig. 1. Time history of elevation steering in a C-band weather radar.

Today's most advanced weather radars applied phased array techniques [11], [12]. Phased array techniques can realize fast scanning to allow tracking of rapidly moving objects, but phased array weather radars do not perform fast scanning but rather observe at multiple angles simultaneously. For example, an X-band phased array weather radar developed in Japan [13] has a wide beam formed in transmission (TX) and narrow beams resolving over a wide angle formed by postprocessing the received signals [14]. The wide TX beam is roughly ten times broader than the narrow reception (RX) beams, which enables observations at ten angles simultaneously. This X-band phased array weather radar, thereby, achieves a scan time of 30 s with observations at all azimuth and elevation angles, giving it the capability to observe extremely hazardous weather phenomena with a horizontal extent of a few hundreds of kilometers and lifetimes of tens of minutes, such as tornadoes, downbursts, and localized thunderstorms [10].

Widely-used nonphased array weather radars observe elevation angles sparsely. For example, Fig. 1 shows the time history of elevation steering of a C-band weather radar operated by the Japan Meteorological Agency (JMA). The radar is steered sparsely over an elevation range of 0–25°, and its elevation steering is particularly sparse for angles more than 5°. The weather radar must maintain each observation elevation angle for one azimuthal rotation, about 15 s.

Manuscript received July 29, 2020; revised September 29, 2020; accepted October 2, 2020. Date of publication October 22, 2020; date of current version July 22, 2021. This work was supported by JSPS KAKENHI under Grant JP17H02069. *(Corresponding author: Eiichi Yoshikawa.)*

Eiichi Yoshikawa is with the Aeronautical Technology Directorate, Japan Aerospace Exploration Agency, Tokyo 181-0015, Japan (e-mail: yoshikawa.eiichi@jaxa.jp).

Tomoo Ushio is with the Department of Electrical, Electronic and Infocommunication Engineering, Osaka University, Osaka 565-0871, Japan.

Hiroshi Kikuchi is with the Center for Space Science and Radio Engineering, The University of Electro-Communications, Chofu 182-8585, Japan.

Digital Object Identifier 10.1109/TGRS.2020.3029875

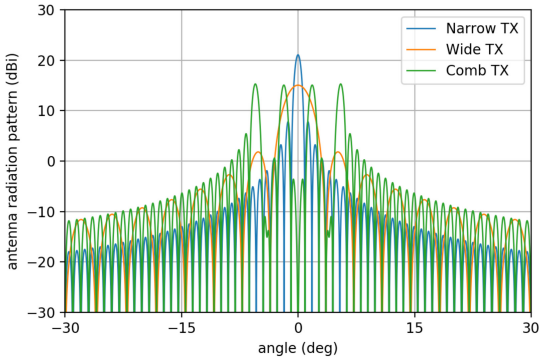

Fig. 2. Antenna radiation pattern profiles of three types of TXs: narrow, wide, and comb.

Although the wide TXs of a phased-array can observe multiple angles simultaneously, the angles must be adjacent. Covering a sparse set of observation elevation angles by wide TXs is inefficient because power is radiated at angles that are not necessary for observation (that is, between pairs of separated observation angles). Furthermore, the combination of a wide TX and a narrow RXs has inferior two-way antenna radiation pattern characteristics to a narrow TX and RX combination. For example, a parabolic antenna typically has a power antenna radiation pattern with a first sidelobe level of −15 or −20 dB (relative to the mainlobe peak), which results in a −30- or −40-dB first sidelobe level in its two-way antenna radiation pattern. On the other hand, the two-way antenna radiation pattern of wide TX antenna has a first sidelobe level −15 or −20 dB since the wide TX cannot contribute sidelobe reductions. With this poorer level, precipitation echo powers at adjacent angles that differ by more than −15 or −20 dB cannot be sufficiently resolved. Such differences in precipitation are associated especially with the extremely hazardous weather. With such precipitation conditions, angles with weak echoes are filled with strong nearby echoes, which can result in misidentification of extremely hazardous weather phenomena.

In this article, the application of comb TX to phased array weather radars is studied by numerical simulation. Fig. 2 shows the antenna radiation pattern profiles of TXs with a narrow, wide, and comb beams. The definition of a comb TX is briefly described in [15]. The comb TX forms multiple mainlobes separately and simultaneously. When a pair of mainlobes are formed further apart than their first sidelobes, their first sidelobe levels in two-way antenna radiation patterns are suppressed more than in the case with a wide TX. Although a higher order sidelobe overlaps another mainlobe, it can be easily mitigated as shown in this article. The methodology of comb beamforming and postprocessing to form receiving beams based on the principle of the phased array antenna theory is described in Section II. In Section III, several example combinations of comb TXs and RXs are investigated and compared with a wide TX. Section IV discusses an application of comb TX to current operational C-band weather radars. In Section V, architecture for realizing comb TX and their applications to various weather radar observations are discussed. Section VI concludes this article.

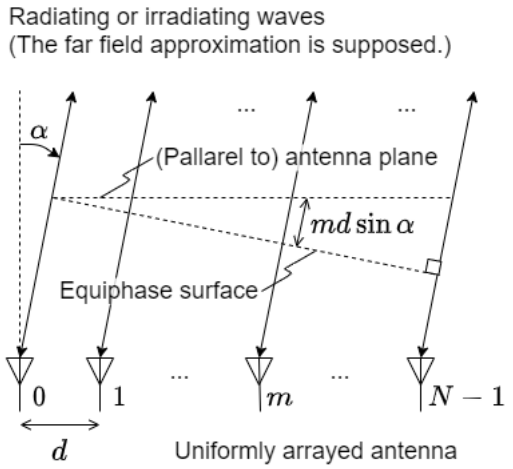

Fig. 3. Geometry of a phased array antenna equation supposed in (1).

II. Methodology

This section begins with the principle of phased array antennas and then explains TX and RX beamforming methods based on this principle. TX beamforming methods include narrow, wide, and comb beamforming, which are hereafter called narrow, wide, and comb TX, respectively. On the other hand, the Fourier and adaptive beamforming are dealt with as reception beamforming methods and are called Fourier and adaptive RX, respectively. This article assumes a receiving system capable of digital beamforming (DBF) processing, which requires digitally sampled signals received individually at antenna elements with time synchronization. These digitized signals are then processed to form RX beams. Since the received signals are saved in a memory device, the DBF processing can be performed any desired number of times in order to form RX beams directed at various angles. The narrow TX and Fourier RX are mathematically the same but are named differently because the simultaneous and multiple beamforming of the DBF is supposed only in RX.

A. Principle of Phased Array Antennas

The formed antenna radiation pattern of a 1-D phased array antenna is a function of amplitudes radiated from elements of the array antenna and has the following discretized formulation [16]:

$$\boldsymbol{y} = \boldsymbol{S}\boldsymbol{x}. \tag{1}$$

The geometry of (1) is shown in Fig. 3. It is assumed that the antenna elements are uniformly arrayed at an interval denoted by d and are omnidirectional. An angle of an antenna radiation pattern is measured from the perpendicular to the antenna plane. $\boldsymbol{x}$ is an N-vector that contains complex amplitudes radiated from antenna elements. $\boldsymbol{y}$ is a vector of complex amplitudes of an antenna radiation pattern that is discretized by N indices. The powers of an antenna radiation pattern are calculated as $\boldsymbol{y} \odot \boldsymbol{y}^*$, where $\odot$ and $\bullet^*$ denote elementwise product and complex conjugate respectively. $\boldsymbol{S}$ is a steering

matrix that is expressed as

$$\boldsymbol{S} = \begin{bmatrix} \boldsymbol{s}_0 & \boldsymbol{s}_1 & \dots & \boldsymbol{s}_l & \dots & \boldsymbol{s}_{N-1} \end{bmatrix}^{\mathrm{T}} \tag{2}$$

where

$$\boldsymbol{s}_l = \begin{bmatrix} s_l^{(0)} & s_l^{(1)} & \dots & s_l^{(m)} & \dots & s_l^{(N-1)} \end{bmatrix}^{\mathrm{T}}$$

and

$$s_l^{(m)} = \frac{1}{\sqrt{N}} \exp\left(-2j\pi m \frac{d}{\lambda} \sin\alpha_l\right).$$

$s_l^{(m)}$ expresses a delay applied to the radiating or irradiating carrier wave on the mth antenna element for directing to the lth angle (α_l). This delay is approximated by assuming that targets exist sufficiently far from the phased array antenna (the far-field approximation). λ is the wavelength of the carrier wave. By defining $\acute{\alpha} = (d/\lambda)\sin\alpha$ and discretizing it as $\acute{\alpha}_l = (l - N/2)/N$, $\boldsymbol{S}$ becomes equivalent to the $N \times N$ Fourier matrix as

$$s_l^{(m)} = \frac{1}{\sqrt{N}} \exp\left(-2j\pi \frac{m(l - N/2)}{N}\right).$$

Strictly speaking, $\boldsymbol{S}$ is a row-switching transformation of the Fourier matrix. These definitions demand that $\boldsymbol{x}$ and $\boldsymbol{y}$ are constrained as follows (see Appendix A):

$$\boldsymbol{x}^{\mathrm{H}}\boldsymbol{x} = \boldsymbol{y}^{\mathrm{H}}\boldsymbol{y} = \frac{2N\lambda}{d} \tag{3}$$

where $\bullet^{\mathrm{H}}$ denotes conjugate transpose.

N is normally defined as $N \gg \hat{N}$, where $\hat{N}$ is the number of actual arrayed antenna's elements. With this definition, the first $\hat{N}$ elements of $\boldsymbol{x}$ are variable, and the other $N - \hat{N}$ elements are constrained to zero. This definition enables $\boldsymbol{y}$ to represent a complex antenna radiation pattern with a fine angular resolution for its mainlobe width.

B. Transmission Beamforming Methods

1) Narrow TX: Complex amplitudes of antenna elements for a narrow TX are determined as

$$\hat{\boldsymbol{x}}_n^{(\mu)} = \sigma \boldsymbol{W}^{(\mu)} \boldsymbol{S}^{\mathrm{H}} \boldsymbol{y}_n \tag{4}$$

where $\boldsymbol{y}_n$ is defined as an N-vector in which a single element corresponding to a desired angle is nonzero and otherwise zero. $\boldsymbol{W}^{(\mu)}$ is the following $N \times N$-matrix:

$$\boldsymbol{W}^{(\mu)} = \begin{bmatrix} \mathrm{diag}\left(\boldsymbol{w}^{(\mu)}\right) & \boldsymbol{O} \\ \boldsymbol{O} & \boldsymbol{O} \end{bmatrix} \tag{5}$$

where $\boldsymbol{w}^{(\mu)}$ is an $\hat{N}$-vector of a window function, the type of which is denoted by the superscript (μ). The rectangular window $\boldsymbol{w}^{(r)}$, in which all the elements are one, derives a beam which is the narrowest realized by $\hat{N}$ antenna elements. A tapered window function $\boldsymbol{w}^{(t)}$ can be applied to reduce the sidelobes of an antenna radiation pattern at the expense of broadening the mainlobe width somewhat. The Taylor window [17] is frequently utilized in arrayed antennas. σ is a factor so that $\hat{\boldsymbol{x}}_n^{(\mu)}$ satisfies (3). A complex antenna radiation pattern formed by $\hat{\boldsymbol{x}}_n^{(\mu)}$ is denoted by $\hat{\boldsymbol{y}}_n^{(\mu)}$, which is calculated by (1).

An example of a narrow TX is shown as a blue line in Fig. 2. For plotting, $\boldsymbol{y}_n$ was set as an element of the 0.0° angle to one, and $\boldsymbol{w}^{(r)}$ was used. A unit of the vertical axis is dBi, that is, the ratio to the power of an omnidirectional antenna in decibels. The power of the omnidirectional antenna is $\boldsymbol{y}^{\mathrm{H}}\boldsymbol{y}/N = 2\lambda/d$. The narrow TX is the fundamental of phased array beamforming.

2) Wide TX: A wide TX can be obtained by applying a narrow-width window function $\boldsymbol{v}^{(\mu)}$ as

$$\hat{\boldsymbol{x}}_w^{(\mu)} = \sigma \boldsymbol{V}^{(\mu)} \boldsymbol{S}^{\mathrm{H}} \boldsymbol{y}_w \tag{6}$$

where, similar to $\boldsymbol{y}_n$, only a single element of $\boldsymbol{y}_w$ is set to nonzero. σ again works for normalizing $\hat{\boldsymbol{x}}_w^{(\mu)}$. Then

$$\boldsymbol{V}^{(\mu)} = \begin{bmatrix} \mathrm{diag}\left(\boldsymbol{v}^{(\mu)}\right) & \boldsymbol{O} \\ \boldsymbol{O} & \boldsymbol{O} \end{bmatrix}. \tag{7}$$

$\boldsymbol{v}^{(\mu)}$ is, for example, a rectangular function with a four times narrower width, in which the first $\hat{N}/4$ elements of $\boldsymbol{v}^{(\mu)}$ are one; otherwise, they are set to zero. (A rectangular window with a width narrower than $\hat{N}$ is denoted by $\boldsymbol{v}^{(r)}$.) This example window leads to a $\hat{\boldsymbol{x}}_w^{(r)}$ that forms a beam four times broader than the $\hat{N}$-width rectangular window. A tapered window function with a narrow width can also be applied. Similar to the narrow TX, its complex antenna radiation pattern $\hat{\boldsymbol{y}}_w^{(\mu)}$ is calculated by substituting $\hat{\boldsymbol{x}}_w^{(\mu)}$ into (1).

An example of a wide TX is shown as an orange line in Fig. 2, which was plotted by setting $\boldsymbol{y}_w$ as an element of the 0.0° angle to one, and applying a four-times narrower $\boldsymbol{v}^{(r)}$. Wide TX is the normal approach used to perform simultaneous multiple-angle observations in phased array weather radars because it can be easily realized just by using a small part of the phased array antenna [13].

3) Comb TX: Complex amplitudes for forming a comb TX are derived as

$$\hat{\boldsymbol{x}}_c^{(\mu)} = \sigma \boldsymbol{W}^{(\mu)} \boldsymbol{S}^{\mathrm{H}} \boldsymbol{y}_c. \tag{8}$$

In $\boldsymbol{y}_c$, multiple elements corresponding to desired multiple angles are nonzero and otherwise zero. Every pair of angles must be displaced from each other so that their mainlobes do not overlap. The complex antenna radiation pattern accomplished by $\hat{\boldsymbol{x}}_c^{(\mu)}$ is calculated by (1) and is denoted by $\hat{\boldsymbol{y}}_c^{(\mu)}$.

A comb TX is exemplified in Fig. 2 as a green line, where $\boldsymbol{y}_c$ as elements of the −5.4°, −1.8°, 1.8°, and 5.4° angles were set to one, and $\boldsymbol{w}^{(r)}$ was used. While the comb TX consists of four replicas of the narrow TX mainlobe, the wide TX has a mainlobe four times broader than that of the narrow TX. This means that their effective widths are the same, and the envelopes of their sidelobe peaks equivalently appear far from the mainlobes.

C. Reception Beamforming Methods

1) Fourier RX: As stated earlier, the Fourier RX is mathematically the same as the narrow TX explained in the previous subsection, that is, it can be formed by following the same procedure. It is important to note that the supposed receiving system allows various reception beams to be formed for a single transmission. Thus, simultaneous multiple-angle observation can be performed with a comb or wide TX.

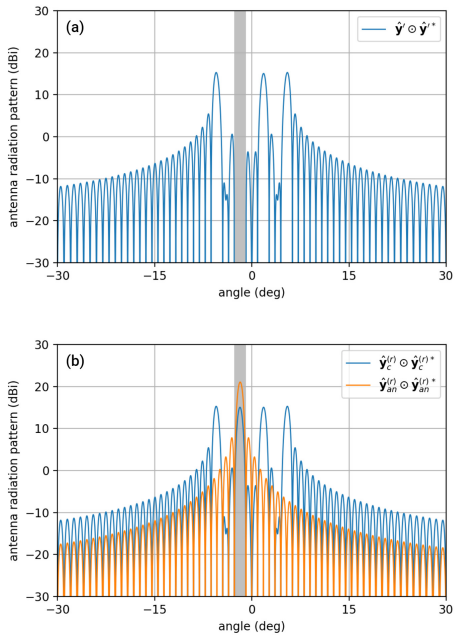

Fig. 4. Example for explaining how to create $\hat{\boldsymbol{y}}'$. (a) $\hat{\boldsymbol{y}}' \odot \hat{\boldsymbol{y}}'^*$. (b) $\hat{\boldsymbol{y}}_c^{(r)} \odot \hat{\boldsymbol{y}}_c^{(r)*}$ and $\hat{\boldsymbol{y}}_{an}^{(r)} \odot \hat{\boldsymbol{y}}_{an}^{(r)*}$. $\hat{\boldsymbol{y}}'$ is created from $\hat{\boldsymbol{y}}_c^{(r)}$ by excluding its elements which corresponds to $\hat{\boldsymbol{y}}_{an}^{(r)}$'s mainlobe (those angles are indicated by the grayed area).

2) Adaptive RX: A reception beam can be formed adaptively to a TX beam, whose complex amplitudes on antenna elements are expressed as

$$\hat{\boldsymbol{x}}_a^{(\mu)} = \sigma \boldsymbol{C} \boldsymbol{W}^{(\mu)} \boldsymbol{S}^{\mathrm{H}} \boldsymbol{y}_a \tag{9}$$

where

$$\boldsymbol{C} = \begin{bmatrix} \left(\boldsymbol{R}^{\mathrm{H}} \boldsymbol{\Sigma}_{y'} \boldsymbol{R}\right)^{-1} & \boldsymbol{O} \\ \boldsymbol{O} & \boldsymbol{O} \end{bmatrix}. \tag{10}$$

$\boldsymbol{R}$ is an $N \times \hat{N}$ matrix that agrees with the first $\hat{N}$ columns of $\boldsymbol{S}$. $\boldsymbol{\Sigma}_{y'}$ is derived from a transmission beam as

$$\boldsymbol{\Sigma}_{y'} = \left(\hat{\boldsymbol{y}}' \hat{\boldsymbol{y}}'^{\mathrm{H}}\right) \odot \boldsymbol{I} \tag{11}$$

where

$$\hat{\boldsymbol{y}}' = \boldsymbol{E} \hat{\boldsymbol{y}}. \tag{12}$$

$\hat{\boldsymbol{y}}$ is the complex antenna radiation pattern of a comb or wide TX, that is, $\hat{\boldsymbol{y}}_c^{(\mu)}$ or $\hat{\boldsymbol{y}}_w^{(\mu)}$. $\boldsymbol{E}$ is a diagonal matrix of the diagonal elements of which those correspond to the mainlobe of $\hat{\boldsymbol{y}}_{an}^{(\mu)}$ are zero, and otherwise one. $\hat{\boldsymbol{y}}_{an}^{(\mu)}$ is a complex antenna radiation pattern formed as a narrow TX based on $\boldsymbol{y}_a$, which is expressed as $\sigma \boldsymbol{S} \boldsymbol{W}^{(\mu)} \boldsymbol{S}^{\mathrm{H}} \boldsymbol{y}_a$. For example, when $\hat{\boldsymbol{y}}$ equals to $\hat{\boldsymbol{y}}_c^{(r)}$ and $\boldsymbol{y}_a$ is defined to direct its second lowest angle mainlobe, as shown in Fig. 2, $\hat{\boldsymbol{y}}'$ is calculated, as shown in Fig. 4(a). As $\hat{\boldsymbol{y}}_c^{(r)}$ and $\hat{\boldsymbol{y}}_{an}^{(r)}$ are plotted in Fig. 4(b), $\boldsymbol{E}$ works to suppress those elements of $\hat{\boldsymbol{y}}_c^{(r)}$ that corresponds to $\hat{\boldsymbol{y}}_{an}^{(r)}$'s mainlobe (those angles are indicated by the grayed area).

III. Performances

A two-way antenna radiation pattern is calculated by the elementwise product of the TX and RX power antenna radiation patterns. This section evaluates the two-way antenna radiation patterns of the comb TX approach and compares them with the wide TX approach. The evaluations were carried out by numerical simulation with the following parameters: the ratio of the antenna element interval to the carrier wavelength d/λ was 0.5, and N and $\hat{N}$ were set to 4096 ($= 128 \times 32$) and 128, respectively.

A. Window Functions and RX Methods

Fig. 5 shows various combinations of a comb TX and a Fourier or adaptive RX. These comb TXs form four mainlobes at angles of $\acute{\alpha} = 0/\hat{N}$, $4/\hat{N}$, $8/\hat{N}$, and $12/\hat{N}$. Four RXs can be formed for each comb TX, and an RX for the lowest angle mainlobe of the comb TX is drawn. ($\acute{\alpha} = 1/\hat{N}$ is a unit angle interval of an arrayed antenna with $\hat{N}$ elements, and signals received from two angles displaced by an integer multiple of $1/\hat{N}$ in the $\acute{\alpha}$-axis are orthogonal to each other. $\acute{\alpha}$ is useful in measuring the properties of antenna radiation patterns because such properties, e.g., mainlobe width, are independent of $\acute{\alpha}$, and the α dependence is simply expressed by the α–$\acute{\alpha}$ relationship, which is indicated in Section II-A as $\acute{\alpha} = (d/\lambda)\sin\alpha$).

Fig. 5(a-1) shows power antenna radiation patterns of a comb TX and a Fourier RX combination with a rectangular window. Fig. 5(a-2) shows a two-way antenna radiation pattern formed by the TX and RX and compares it with a reference formed by a combination of a narrow TX and Fourier RX directed to the same angle. This reference can be considered as a pattern representative of a conventional weather radar. The comparison indicates that the comb TX–Fourier RX combination has a mainlobe peak level lower than the reference because the comb TX distributes TX power to the four mainlobes. Meanwhile, the first sidelobe levels are roughly -25 and -40 dB, which are respectively similar to and lower than the reference. However, the comb TX–Fourier RX combination has large sidelobes at the angles of the other three mainlobes of the comb TX (in an angular range of 0°–15°), which are from -35 to -25 dB compared with the mainlobe peak.

As is well-known, sidelobes can be suppressed by adopting a window function, an example of which shown in Fig. 5(b-1) and (b-2). Here, the Taylor window function was applied to both the comb TX and the Fourier RX. The two parameters that specify the Taylor window, a design sidelobe ratio and $\bar{n}$, were set to 25 dB and 5, respectively. As shown in Fig. 5(b-1), the mainlobes of the comb TX and Fourier RX became wider than that in Fig. 5(a-1) due to the tapered window, but their sidelobes were meanwhile suppressed. In the Fourier RX, the first sidelobe level is, as designed, -25 dB from the mainlobe peak. In the comb TX, the four mainlobe peaks were reduced similar to Fig. 5(a-1), and the first sidelobe (on the lower side of the lowest angle mainlobe and on the higher side of the highest-angle mainlobe) was almost equal to that of the Fourier RX. Fig. 5(b-2) shows the two-way antenna radiation pattern for the lowest angle mainlobe of the comb TX. High sidelobes due to the other mainlobes were reduced by about 5 dB compared with Fig. 5(a-2).

Fig. 5(c-1) and (c-2) did not use a window function but instead employed the adaptive RX. The same comb TX was used in Fig. 5(a-1) and (c-1). The adaptive RX forms a pattern

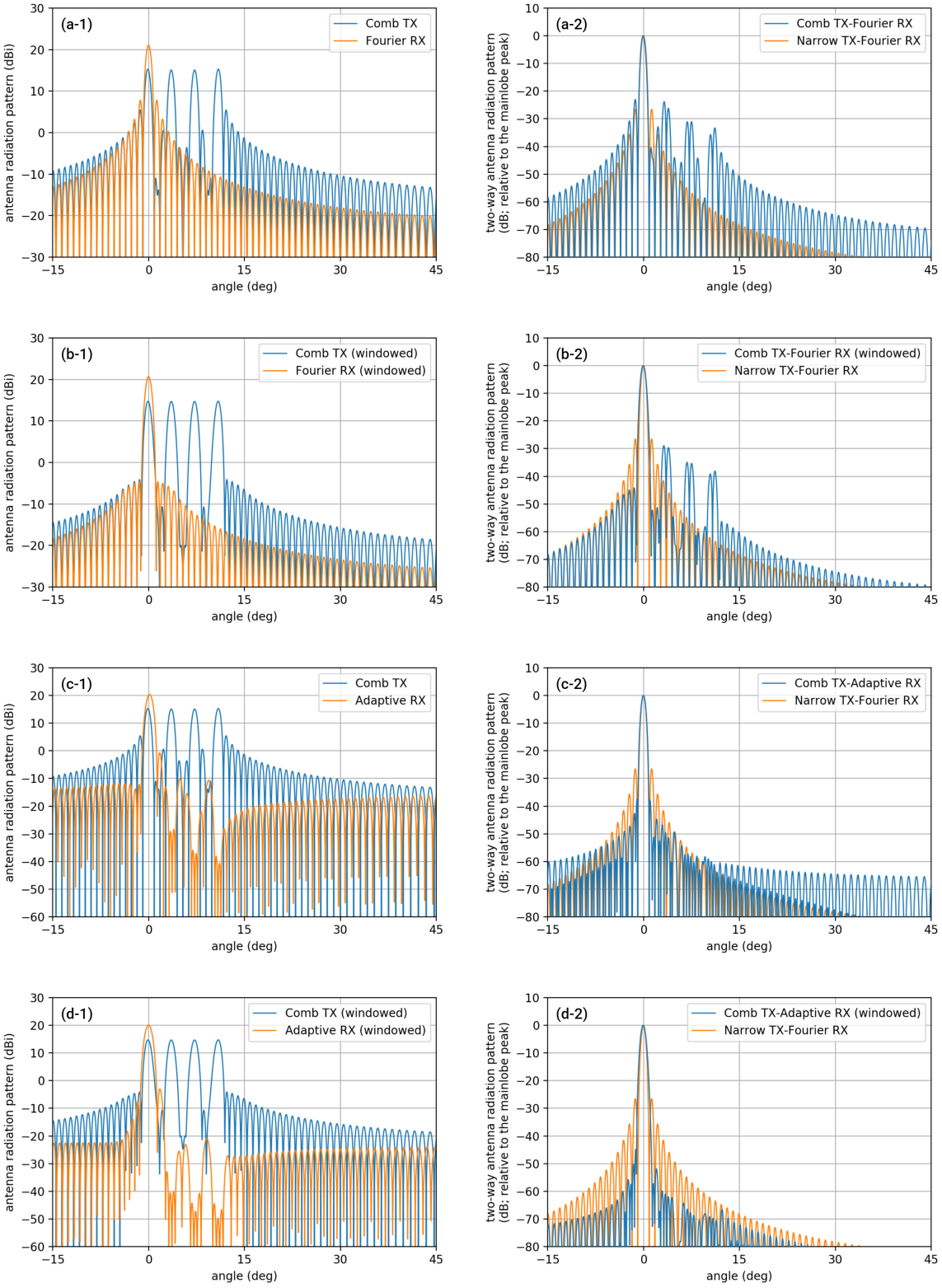

Fig. 5. Various combinations of a Comb TX and a Fourier or adaptive RX. (a) Comb TX–Fourier RX. (b) Comb TX–Fourier RX both Taylor windowed. (c) Comb TX–adaptive RX. (d) Comb TX–adaptive RX, both Taylor windowed. *-1) and *-2) show transmission and reception antenna radiation patterns and two-way antenna radiation pattern, respectively.

to direct the angle of the lowest angle mainlobe of the comb TX and reduced sidelobes drastically at the angles of the other three mainlobes. In its two-way antenna radiation pattern, as shown in Fig. 5(c-2), the mainlobe is not broadened, and high sidelobes due to the other mainlobes of the comb TX do not appear. Both the lower and higher side first sidelobes are

narrower than those in Fig. 5(a-2) and (b-2) and are greatly superior to the conventional weather radar (about −35 dB relative to the mainlobe peak). Since the narrow-width first sidelobes overlap the mainlobe, they can be considered as a part of the mainlobe, and the second sidelobes then have the same effect as the first sidelobes of a normal pattern. The higher of the two second sidelobes is less than −45 dB relative to the mainlobe peak, which should have almost no effect on weather radar observations. On the other hand, sidelobe levels diminish more slowly along the angle axis compared with the reference. Roughly, at angles less than −5 or more than 10°, the sidelobe peak levels of the comb TX–adaptive RX combination are higher than the reference case. At those angles, however, the sidelobe peak levels are almost less than −55 dB, which should be negligible in actual observations.

As shown in Fig. 5(d-1) and (d-2), a window function can be applied to both a comb TX and adaptive RX. Here, the same window function as Fig. 5(b-1) and (b-2) is applied. With the comb TX, sidelobe levels are reduced instead of mainlobe broadening, as seen in Fig. 5(b-1). The adaptive RX's mainlobe is broadened by the window function, and the adaptive scheme reduces sidelobes especially at the angles of the other mainlobes of the comb TX. Fig. 5(d-2) shows a two-way antenna radiation pattern in which sidelobe levels are greatly suppressed compared with the reference.

It should be noted that a lower phase noise of an arrayed antenna is demanded to realize a lower sidelobe level. When σ_p (rad) is defined as the standard deviation of the zero-mean Gaussian phase error of each antenna element, the phase error gives a lower limit in a power antenna radiation pattern of $20\log_{10}\sigma_p$ dBi (see details in Appendix B). That is, in order to realize a sidelobe level of −40 dBi, which is almost the lowest sidelobe level seen in the adaptive RX of Fig. 5(c-1), a value of $\sigma_p = 0.01$ is needed.

B. Comb TX Specifications

The previous section revealed that adaptive RXs are promising for realizing weather radars with the comb TX approach. This section investigates their performances depending on comb TX's specifications. Especially, comb TXs forming two, four, and eight mainlobes are supposed. In addition, angle intervals are set as $\acute{\alpha} = 2/\hat{N}$, $4/\hat{N}$, $6/\hat{N}$, or $8/\hat{N}$, and the lowest angle mainlobe is set to an angle of 0° ($\acute{\alpha} = 0$). Fig. 5(c-1) shows a case with four mainlobes at an interval of $4/\hat{N}$, and Fig. 6 shows its four two-way antenna radiation patterns.

The performance was evaluated with respect to mainlobes and sidelobes. The methods for calculating the performance properties are explained in the following using the case of Fig. 6 as an example. Mainlobes were evaluated by their peak levels and widths. Mainlobe peak level and width are defined as the minimum and the maximum values of the four mainlobes, respectively. The mainlobe width is a difference between the two angles measured in the $\acute{\alpha}$-axis at which power is −3 dB from the mainlobe peak. Sidelobes were evaluated by their maximum sidelobe levels and −60-dB angle from the mainlobe peak. For the maximum sidelobe level, the maximum level of sidelobe peaks of four two-way antenna radiation pattern was adopted. The −60-dB angle, again measured in the $\acute{\alpha}$-axis, is the maximum of the four angles, each of which is the furthest angle of sidelobe peak at which the level is more than −60 dB relative to the mainlobe peak in a two-way antenna radiation pattern. Note that only sidelobe peaks in a practical angle range of −5–90° are considered.

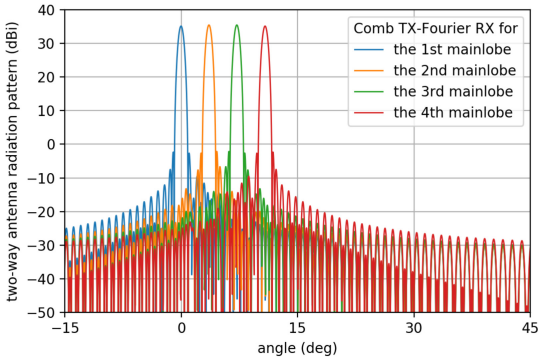

Fig. 6. Four two-way antenna radiation patterns formed by the combination of a comb TX and adaptive RX shown in Fig. 5(c-1).

Fig. 7(a) and (b), respectively, shows the evaluated mainlobe and sidelobe properties of the two-way antenna radiation patterns. Their horizontal axes indicate mainlobe intervals, and the leftmost and rightmost horizontal axis values correspond to a wide and narrow TX, respectively. The numbers of mainlobes are indicated by the colors of the lines. Fig. 7(a) and (b) shows that with the comb TX approach, the mainlobe properties depend only on the number of mainlobes, not on the interval, while the sidelobe properties get worse with a larger number of mainlobes or a smaller mainlobe interval. More specifically, the mainlobe peak levels do not greatly vary with the mainlobe interval, but they are reduced by increasing the number of mainlobes. This is due to the definition of the comb TX approach that distributes the transmission power over the multiple mainlobes. The mainlobe width is almost independent both of the number of mainlobes and the mainlobe interval and is equivalent to a narrow TX with values from $\acute{\alpha} = 0.0066$ to 0.0073 corresponding to between $\alpha = 0.76°$ and 0.84° around the angle perpendicular to the antenna plane. (The conversion from $\acute{\alpha}$ to α (deg) around the perpendicular angle is calculated by $\alpha = 2\sin^{-1}((\lambda/d)(\acute{\alpha}/2)/N)$, which can be derived from the principle.) The sidelobe properties rapidly improve from $2/\hat{N}$ to $4/\hat{N}$ mainlobe intervals and become comparable to the narrow TX when the mainlobe interval is equal to or greater than $4/\hat{N}$. The comb TX with four mainlobes and a $4/\hat{N}$ interval achieves a maximum sidelobe level of −37 dB and a −60-dB angle of $\acute{\alpha} = 0.1199$ (13.77° around the perpendicular angle).

Fig. 7 also compares wide TXs with the comb TXs and shows that the wide TXs are worse than the comb TXs in all evaluation properties. The poor properties of sidelobes are consistent with the trend of the comb TXs in which the sidelobe properties are deteriorated by a lower mainlobe interval. Also, with respect to the mainlobe properties, the wide TXs are worse than the comb TXs. As seen in Fig. 8, which shows (a) power antenna radiation patterns of the wide TX

TABLE I
NUMBER OF PPI SCANS PER MINUTE

Elevation angle (deg)	0.0	0.3	0.7	1.0	1.1	1.7	2.0	2.5	3.5	3.8	4.8	6.7	9.3	12.9	17.9	25.0
Non-comb radar	0.24	0.49	0.24	0.24	0.24	0.24	0.24	0.12	0.12	0.24	0.12	0.12	0.12	0.12	0.12	0.12
Comb radar	1	1	1	1	1	1	1	1	1	1	1	1	1	1	1	1

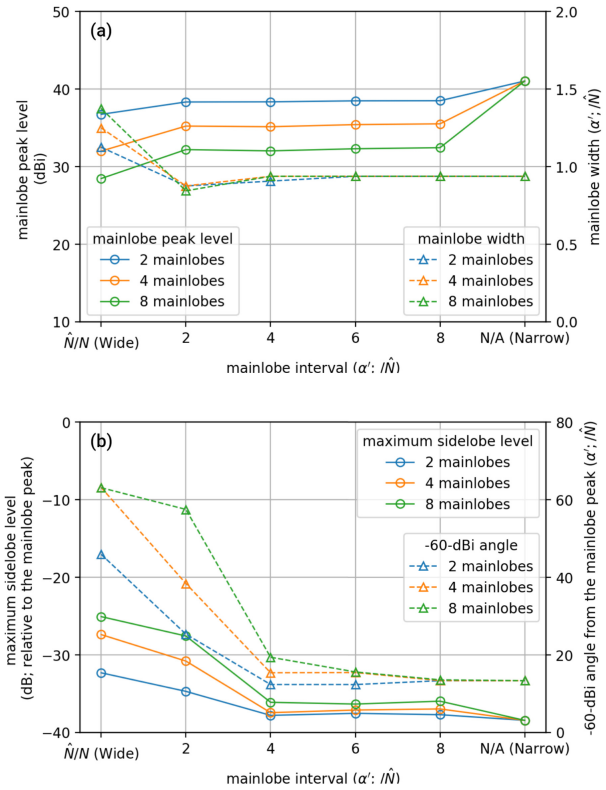

Fig. 7. Characteristics of two-way antenna radiation patterns evaluated on (a) mainlobe and (b) sidelobes.

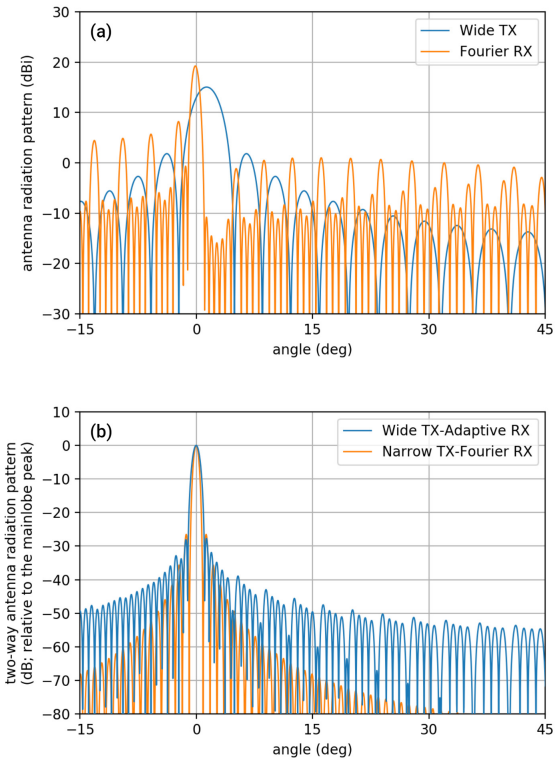

Fig. 8. Combination of a wide TX and an adaptive RX. (a) and (b) Transmission and reception antenna radiation patterns and two-way antenna radiation pattern, respectively.

and an adaptive RX for the lowest angle of the wide mainlobe and (b) their two-way antenna radiation pattern (which is compared with a reference formed by a combination of a narrow TX and Fourier RX), the wide TX beam does not contribute to sharpening mainlobe of the two-way antenna radiation pattern and has low levels at the edges of its wide mainlobe.

IV. APPLICATION AT A C-BAND FREQUENCY

We now discuss adding the comb TXs and adaptive RXs to conventional C-band weather radars. In order to steer all elevation angles of a conventional noncomb radar (see Fig. 1), four comb TXs that each direct four mainlobes can be used, as shown in Fig. 9. Here, it is assumed that the comb radar takes 15 s for a single azimuthal rotation, which is equivalent to the noncomb radar. Compared with Fig. 1 in which the noncomb radar takes almost 500 s for a volume scan, the comb radar takes just 60 s. The noncomb radar's volume scan time of almost 500 s comprises 26 PPI scans, each of which takes about 15 s, and the time to mechanically change the antenna elevation angle, which is totally about 100 s. In contrast,

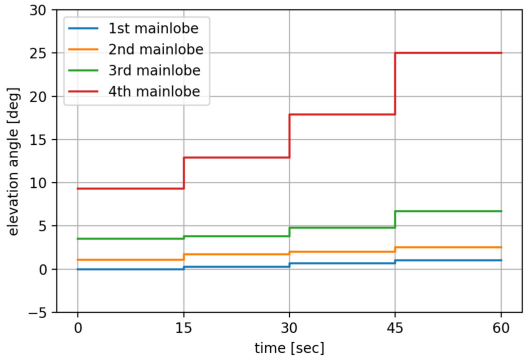

Fig. 9. Time history of elevation steering of a C-band weather radar with comb TXs and adaptive RXs.

the comb radar acquires four PPI scans simultaneously, and its electronic beam steering eliminates the time needed to change elevation angle. Table I compares the number of PPI scans that can be performed in one minute between the noncomb and comb radars. At each PPI elevation, the comb TX and

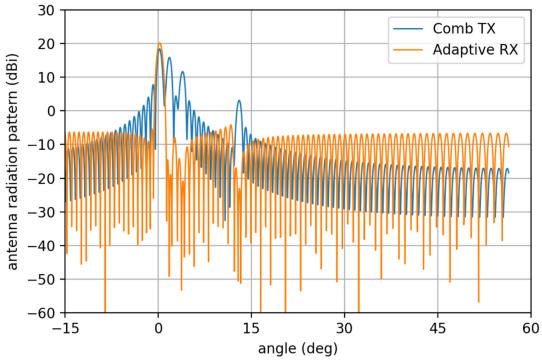

Fig. 10. Antenna radiation patterns of a comb TX and adaptive RX applied to C-band weather radar.

adaptive RX function enables the C-band weather radar to scan two to eight times more frequently.

Antenna radiation patterns were simulated with $\hat{N} = 128$ and $N = 128 \times 32$. The 128 antenna elements were assumed to be arrayed at a uniform interval of $d/\lambda = 0.6$. For both the comb TXs and adaptive RXs, a Taylor window was used with a design sidelobe ratio of 20 dB and $\bar{n} = 4$. When assuming a radar carrier frequency of 5.35 GHz, the (longitudinal) size of the arrayed antenna is about 4.3 m. Fig. 10 shows the power antenna radiation patterns of a comb TX and an adaptive RX. The comb TX directs four mainlobes at angles of 0.00°, 1.09°, 3.51°, and 9.29°, which corresponds to the first comb TX of the comb radar (differences of 0.01° from the angles shown in Table I are the result of the digitization of the angle axis). The adaptive RX is for the lowest angle mainlobe of the comb TX. The mainlobe peak levels of the comb TX are adjusted considering maximum ranges for each mainlobe angle. While C-band weather radars are typically designed to radiate an electric power to cover out to 400 km range, such power is not necessarily high elevation angles because weather phenomena occur in the troposphere ($<$ 15-km height). When assuming the $4/3$ earth model of electromagnetic wave propagation [18], while 0.00° elevation angle and 400-km distance are still in the troposphere, 9.29° elevation angle and 90-km distance reach to a height of 15 km. Since received power is proportional to the inverse square of the distance (neglecting attenuation on the propagation path), the mainlobe peak level at 9.29° elevation can be reduced by about −13 dB compared with that at 0.00°.

The two-way antenna radiation patterns of the first–fourth comb TXs are shown in Fig. 11(a)–(d), respectively. The mainlobe widths of the two-way antenna radiation patterns are 0.0076–0.0085 in $\acute{\alpha}$, which corresponds to 0.72°–0.82° in α around the perpendicular angle. These mainlobe widths are comparable to the 0.70° mainlobe width of the conventional C-band radar. The first sidelobe levels are less than −35 dB relative to the mainlobe peaks. The −60-dB angles are from 0.0427–0.1199 in $\acute{\alpha}$, which corresponds to 3.92°–11.01° in α around the perpendicular angle. Fig. 12(a) and (b) shows power antenna radiation patterns of a comb TX and adaptive RX of which first and fourth patterns of Fig. 11(d), respectively, consist. Compared with the adaptive RX of Fig. 12(a), the sidelobes of the adaptive RX of Fig. 12(b) fall below

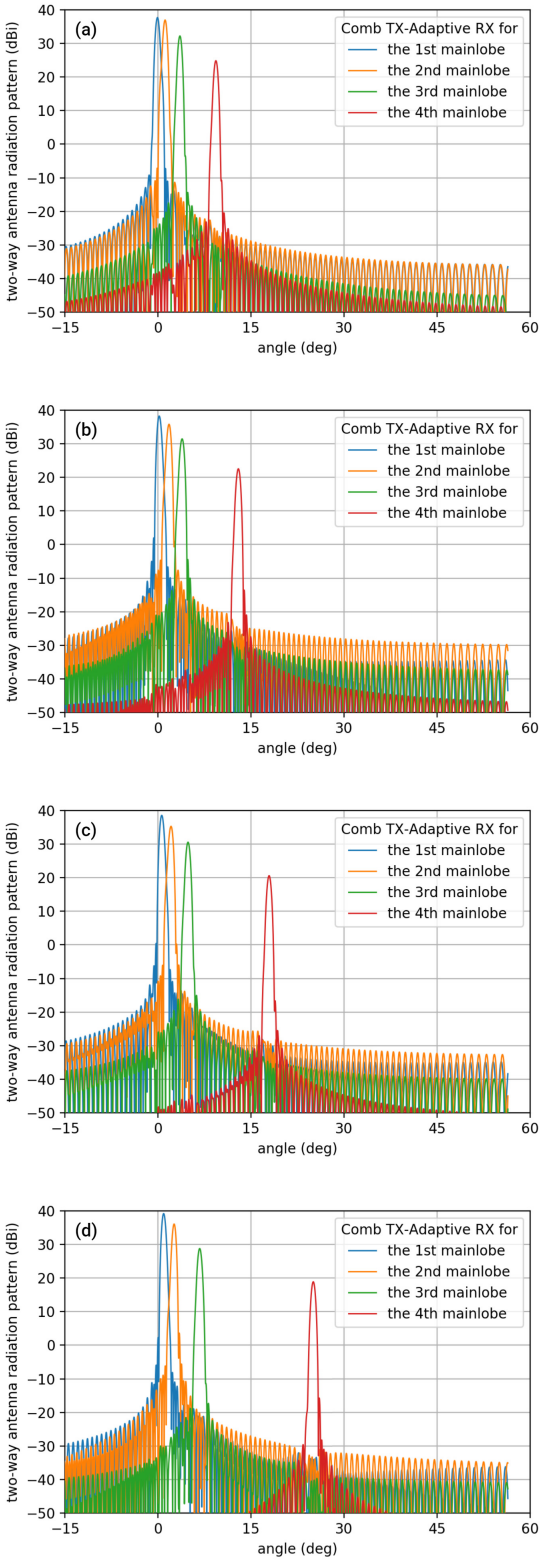

Fig. 11. Two-way antenna radiation patterns for a C-band weather radar application. (a)–(d) correspond to the first–fourth comb TXs scheduled, respectively, as in Fig. 9.

−60 dBi (see angles at a few degrees.) This is mainly because the peak level of the fourth mainlobe is roughly −20 dB smaller than that of the first mainlobe. In order to relax phase

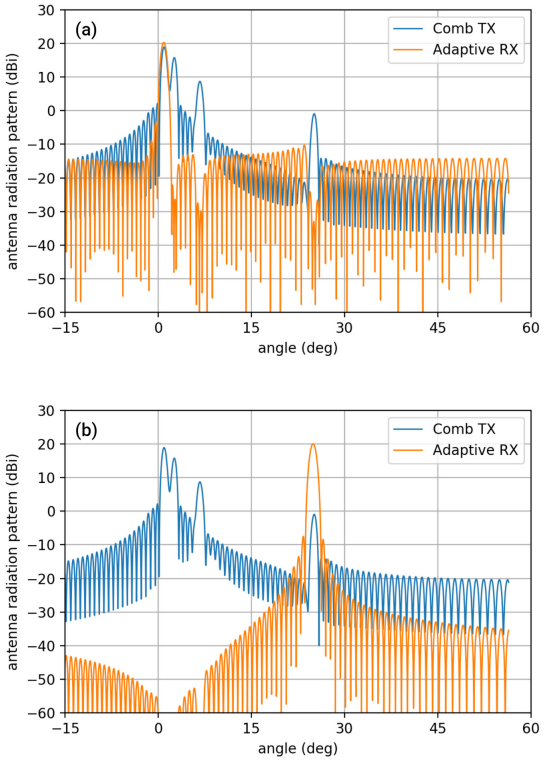

Fig. 12. Power antenna radiation patterns of a comb TX and adaptive RX that form (a) first pattern of Fig. 11(d) and (b) fourth pattern of Fig. 11(d).

noise accuracy to realize such a low sidelobe level, the fourth mainlobe peak level can be increased.

V. Discussion

Although the comb TX can be used for sparse-angle observations, an angular range of 0°–90° can be fully covered by several comb TXs, as it is filled by several wide TXs. Since the two-way antenna radiation pattern properties of the comb TXs are superior to those of the wide TXs, as shown in Section III, the comb TX approach is also useful for full-angle observations. The comb TX is also as easy to manufacture as a wide TX. A wide TX is simply realized by feeding antenna elements in a small part of an arrayed antenna, while, on the other hand, a comb TX can form mainlobes with a uniform level and interval by alternately feeding and skipping antenna elements in a certain ratio (e.g., feeding the first n elements of the array for a wide TX, or feeding the first element of each n sets of elements in the array for a comb TX). When the numbers of fed antenna elements are the same, as being understood from Fig. 2, the same number of comb or wide TXs is required for a full-angle scan. (In order to form mainlobes arbitrarily as in Section IV, the comb TX approach requires all antenna elements to be activated.)

There is a tradeoff between sparse-angle and full-angle observations. Full-angle observation does not miss any weather phenomena spatially but takes a longer time to complete a volume scan. It can be considered that full-angle observation is suitable for short-range (tens of kilometer) radars because such short-range radars have recently been in demand in urbanized areas for the early detection and warning of severe weather phenomena. For this purpose, it is important to detect small initiations of phenomena with no missing areas by a full-angle scan. Moreover, since shorter range radar observations take less time, the time saved by the shorter observation range can be used to achieve full-angle observation.

On the other hand, sparse-angle observation achieves a faster volume scan but can miss weather phenomena between the mainlobes. This can be thought of as suitable for long-range radars (hundreds of kilometers) because the resolution volume becomes larger at further distances, which reduces the "miss" rate for detecting severe weather phenomena. Furthermore, current weather prediction and practical applications assume sparse-angle observations and have already made great contributions [19]–[21]. Even upgrading just the scan rate using the comb TX approach would bring improvements and could be easily introduced to current weather prediction and practical applications.

VI. Conclusion

Phased array technologies have recently been applied in weather radar engineering. In contrast to applications that detect and track multiple moving objects, weather radars use phased array techniques to observe multiple angles simultaneously. Existing phased array weather radars apply a wide TX–Fourier RX combination and achieve scanning of a wide continuous elevation angle range. However, the wide TX constrains the multiple observation angles to be adjacent. The question "what if this restriction is removed?" provided the impetus for this study.

Numerical simulations of various combinations of a TX and RX revealed that combinations of comb TXs and adaptive RXs can form two-way antenna radiation patterns with mainlobe and sidelobe properties comparable to a conventional weather radar (the narrow TX–Fourier RX). In numerical simulations with 128 antenna elements and $d/\lambda = 0.5$, the mainlobe and sidelobe properties of two-way antenna radiation patterns formed by the comb TX approach were degraded by increasing the number of mainlobes or by reducing the mainlobe interval. A comb TX that directs four mainlobes with a mainlobe interval of $4/\hat{N}$ (in $\acute{\alpha}$) achieved a mainlobe peak level of 35 dBi and a mainlobe width of 0.85°. Furthermore, its maximum sidelobe level was less than −37 dB relative to the mainlobe peak level, and its sidelobe level reached −60 dB at angles of 13.77° (at most) from the mainlobe peak. (The mainlobe peak level is not as high as the conventional weather radar by the definition of the comb TX approaches. The reduction can be compensated by increasing the feeding power.)

Observation by a C-band weather radar equipped with a comb TX was then simulated. By using four comb TXs that form four mainlobes, the volume scan time of a conventional C-band radar, which is almost 500 s, was reduced to 1 min while giving comparable mainlobe and sidelobe properties: a mainlobe width of 0.72°–0.82°, a sidelobe level less than −35 dB, and a −60 dB angle of 3.92°–11.01 ° (sidelobe properties are measured relative to mainlobe peak, and angles are measured around the perpendicular angle). Note that this

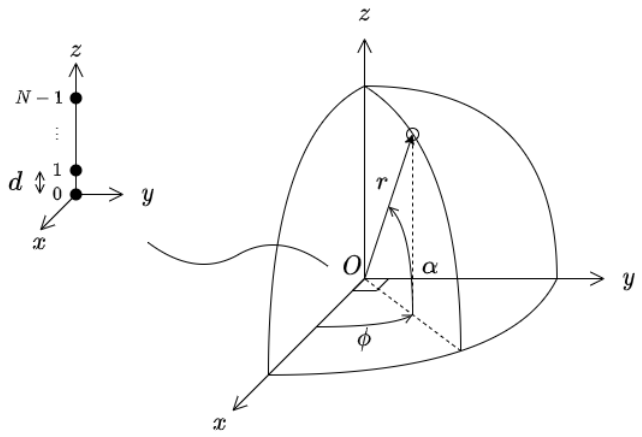

Fig. 13. 1-D arrayed antenna on a spherical coordinate system.

simulation adaptively sets the mainlobe peak levels to ranges necessary to observe the troposphere in order to be efficient in TX power use. These properties were derived by 128 antenna elements with $d/\lambda = 0.6$ and demanded an antenna size of 4.3 m

The comb TX approach can be used not only for sparse-angle observation but also for full-angle observation. Compared with the wide TX approach, which is currently the conventional method used for full-angle observation, the comb TX approach is superior in its mainlobe and sidelobe properties. Moreover, both approaches are similar in their manufacturing demands. It can be considered that sparse- and full-angle observations are advantageous for long-range (hundreds of kilometers) and short-range (tens to one hundred kilometers) observations, respectively, and the comb TX approach is useful for both types of observation.

Appendix A
Normalization of a Discretized Antenna Radiation Pattern

Let us place a 1-D phased array antenna with N elements on a spherical coordinate system, as shown in Fig. 13. The zeroth antenna element is placed at the origin of the spherical coordinates, and other antenna elements are lined up in the positive direction on the z-axis. Each pair of adjacent antenna elements is displaced with an interval, which is sufficiently small (by which the phased array antenna is approximately placed at the origin). In the spherical coordinate system, azimuth and elevation angles are denoted by ϕ and α, respectively. When $y(\phi, \theta)$ denotes complex amplitudes of a (continuous) antenna radiation pattern, its integration for whole angles is 4π sr by its definition [22], which is expressed as

$$\int_{-\pi}^{\pi} \int_{-\frac{\pi}{2}}^{\frac{\pi}{2}} |y(\phi, \alpha)|^2 \cos\alpha d\alpha d\phi = 4\pi. \tag{13}$$

Since $y(\phi, \alpha)$ of the 1-D phased array antenna is obviously isotropic with respect to ϕ, it can be reduced to

$$\frac{1}{2} \int_{-\frac{\pi}{2}}^{\frac{\pi}{2}} |y(\alpha)|^2 \cos\alpha d\alpha = 1. \tag{14}$$

Introducing a variable conversion to represent (1) as a Fourier transformation, $(d/\lambda)\sin\alpha = \acute{\alpha}$, and its differential $(d/\lambda)\cos\alpha d\alpha = d\acute{\alpha}$

$$\frac{d}{2\lambda} \int_{-\frac{d}{\lambda}}^{\frac{d}{\lambda}} |\acute{y}(\acute{\alpha})|^2 d\acute{\alpha} = 1 \tag{15}$$

where $\acute{y}(\acute{\alpha}) = y(\alpha)$. By digitizing $\acute{\alpha}_l = (l - N/2)/N$ and $l = 0, 1, \ldots, N-1$ as in (1), (15) is approximated as

$$\frac{d}{2N\lambda} \sum_{l=0}^{N-1} |\acute{y}(\acute{\alpha}_l)|^2 = 1. \tag{16}$$

Since $\acute{y}(\acute{\alpha}_l)$ is equivalent to the lth element of $\boldsymbol{y}$ of (1), (16) can be rewritten as $\boldsymbol{y}^{\mathrm{H}}\boldsymbol{y} = 2\ N\lambda/d$. In addition, (1) leads to $\boldsymbol{x}^{\mathrm{H}}\boldsymbol{x} = \boldsymbol{y}^{\mathrm{H}}\boldsymbol{y} = 2\ N\lambda/d$.

It is clear by the principle of the Fourier transform that the radiated antenna pattern aliases in $\acute{\alpha} < -1/2$ or $\acute{\alpha} \geq 1/2$. In theory, therefore, the antenna element interval is set to half of the carrier wavelength. Some actual phased array antennas are designed as $d/\lambda > 1/2$ when it is technically difficult to narrow the antenna element interval. Such antennas are operated so that the aliased part of the antenna radiation pattern is sufficiently small. When $d/\lambda < 1/2$, on the other hand, $\acute{y}(\acute{\alpha}_l)$ of (16) should be zero in $\acute{\alpha}_l < -1/2$ or $\acute{\alpha}_l \geq 1/2$.

Appendix B
Phase Noise Effect on Phased Array Antenna Radiation Patterns

The lth angle of a power antenna radiation pattern can be calculated by

$$p_l = {y_l}^* y_l. \tag{17}$$

Here, let us define y_l as its complex amplitude affected by phase noises as

$$y_l = \boldsymbol{s}_l^{\mathrm{T}} \operatorname{diag}(\boldsymbol{v})\boldsymbol{x} \tag{18}$$

where $\boldsymbol{v}$ is an N-vector and the mth element $v^{(m)}$ denotes a phase noise on the mth antenna element as

$$v^{(m)} = \exp\left(j\theta^{(m)}\right). \tag{19}$$

$\theta^{(m)}$ is assumed as a Gaussian random variable that satisfies $E[\theta^{(i)}] = 0$ and $E[{\theta^{(i)}}^2] = \sigma_p^2$. σ_p (rad) is a standard deviation of the phase noises. Furthermore, it can be assumed that phase noises of two different antenna elements are independent as $E[\theta^{(i)}\theta^{(j)}] = 0$. By the second-order Maclaurin series approximation of p_l with respect to $\{\theta^{(i)}\}$, its expectation can be expressed as

$$E[p_l] \approx \left(\boldsymbol{s}_l^{\mathrm{T}}\boldsymbol{x}\right)^* \left(\boldsymbol{s}_l^{\mathrm{T}}\boldsymbol{x}\right) + \sigma_p^2 \sum_m \Re\left[-s_l^{(m)*} x^{(m)*} \left(\boldsymbol{s}_l^{\mathrm{T}}\boldsymbol{x} - s_l^{(m)} x^{(m)}\right)\right]. \tag{20}$$

The first and second terms of (20) correspond to the zeroth- and second-order terms of the Maclaurin series, respectively. (The first-order term vanishes because it contains the expectation of $\{\theta^{(i)}\}$, that is, zero-mean Gaussian.) The first term of (20) represents a component, which is free from the phase noises. Meanwhile, the second term is the other additional

component brought by the phase noises and can be used as a lower limit of $E[p_l]$.

When $\boldsymbol{s}_l^{\mathrm{T}}\boldsymbol{x} \approx 0$ (in other words, at an angle where antenna sidelobe level is needed to be reduced), the second term is dominant in $E[p_l]$. With this condition, (20) can be approximately estimated as

$$E[p_l] > \min\{E[p_l]\} \approx \sigma_p^2 \sum_m s_l^{(m)*} x^{(m)*} s_l^{(m)} x^{(m)} = 2\sigma_p^2 \frac{\lambda}{d} \tag{21}$$

where the definitions of $s_l^{(m)*} s_l^{(m)} = N^{-1}$ and $\boldsymbol{x}^{\mathrm{T}}\boldsymbol{x} = 2\ N\lambda/d$ were substituted. The (approximate) lower limit is, in dBi, a function just of σ_p as

$$\min\{E[p_l]\} \approx 20\log_{10}\sigma_p \quad \text{(dBi)}. \tag{22}$$

REFERENCES

[1] T. D. Crum and R. L. Alberty, "The WSR-88D and the WSR-88D operational support facility," *Bull. Amer. Meteorolog. Soc.*, vol. 74, no. 9, pp. 1669–1687, Sep. 1993.

[2] N. Kodaira and J. Aoyagi, "History of radar meteorology in Japan," in *Radar in Meteorology*, D. Atlas, Ed. Boston, MA, USA: American Meteorological Society, 1990.

[3] D. McLaughlin *et al.*, "Short-wavelength technology and the potential for distributed networks of small radar systems," *Bull. Amer. Meteorolog. Soc.*, vol. 90, no. 12, pp. 1797–1818, Dec. 2009.

[4] F. Junyent and V. Chandrasekar, "Theory and characterization of weather radar networks," *J. Atmos. Ocean. Technol.*, vol. 26, no. 3, pp. 474–491, Mar. 2009.

[5] E. Yoshikawa, T. Ushio, Z. Kawasaki, and V. Chandrasekar, "Dual-directional radar observation for preliminary assessment of the ku-band broadband radar network," *J. Atmos. Ocean. Technol.*, vol. 29, no. 12, pp. 1757–1768, Dec. 2012.

[6] V. Chandrasekar, H. Chen, and B. Philips, "DFW urban radar network observations of floods, tornadoes and hail storms," in *Proc. IEEE Radar Conf. (RadarConf)*, Apr. 2018, pp. 0765–0770.

[7] V. Chandrasekar and S. Lim, "Retrieval of reflectivity in a networked radar environment," *J. Atmos. Ocean. Technol.*, vol. 25, no. 10, pp. 1755–1767, Oct. 2008.

[8] S. Shimamura, V. Chandrasekar, T. Ushio, G. Kim, E. Yoshikawa, and H. Chen, "Probabilistic attenuation correction in a networked radar environment," *IEEE Trans. Geosci. Remote Sens.*, vol. 54, no. 12, pp. 6930–6939, Dec. 2016, doi: 10.1109/TGRS.2016.2592532.

[9] E. Yoshikawa, V. Chandrasekar, T. Ushio, and T. Matsuda, "A Bayesian approach for integrated raindrop size distribution (DSD) retrieval on an X-band dual-polarization radar network," *J. Atmos. Ocean. Technol.*, vol. 33, no. 2, pp. 377–389, Feb. 2016, doi: 10.1175/JTECH-D-15-0060.1.

[10] R. A. House, Jr., *Cloud Dynamics*. New York, NY, USA: Academic, 1993, ch. 4, pp. 107–129.

[11] J. Wurman and M. Randall, "An inexpensive mobile rapid-scan radar," *Proc. 30th Int. Conf. Radar Meteorol.*, p. 3.4, 2001.

[12] H. B. Bluestein, M. M. French, I. PopStefanija, R. T. Bluth, and J. B. Knorr, "A mobile, phased-array Doppler radar for the study of severe convective storms," *Bull. Amer. Meteorolog. Soc.*, vol. 91, no. 5, pp. 579–600, May 2010.

[13] F. Mizutani *et al.*, "Fast-scanning phased-array weather radar with angular imaging technique," *IEEE Trans. Geosci. Remote Sens.*, vol. 56, no. 5, pp. 2664–2673, May 2018, doi: 10.1109/TGRS.2017.2780847.

[14] E. Yoshikawa *et al.*, "MMSE beam forming on fast-scanning phased array weather radar," *IEEE Trans. Geosci. Remote Sens.*, vol. 51, no. 5, pp. 3077–3088, May 2013, doi: 10.1109/TGRS.2012.2211607.

[15] E. Yoshikawa and T. Ushio, "Comb imaging on a phased array weather radar," in *Proc. Workshop Circuits Syst.*, vol. 32, 2019, pp. 138–141.

[16] R. C. Hansen, *Phased Array Antennas*, 2nd ed. Hoboken, NJ, USA: Wiley, 2009.

[17] T. T. Taylor, "Design of line-source antennas for narrow beamwidth and low side lobes," *Trans. IRE Prof. Group Antennas Propag.*, vol. 3, no. 1, pp. 16–28, Jan. 1955, doi: 10.1109/TPGAP.1955.5720407.

[18] R. J. Doviak and D. S. Zrnic, *Doppler Radar and Weather Observations*, 2nd ed. New York, NY, USA: Dover, 1993.

[19] B. Macpherson *et al.*, "Assimilation of radar data in numerical weather prediction (NWP) models," in *Weather Radar, Principles and Advanced Applications*, P. Meischner, Ed. Berlin, Germany: Springer-Verlag, 2004, Ch. 9.

[20] F. Fabry, *Radar Meteorology*. Cambridge, U.K.: Cambridge Univ. Press, 2015.

[21] E. Yoshikawa and T. Ushio, "Tactical decision-making support information for aircraft lightning avoidance: Feasibility study in area of winter lightning," *Bull. Amer. Meteorol. Soc.*, vol. 100, pp. 1443–1452, 2019, doi: 10.1175/BAMS-D-18-0078.1.

[22] K. Marhefka, *Antennas: For All Applications*, 3rd ed. New York, NY, USA: McGraw-Hill, 2003.

Eiichi Yoshikawa received the B.E. degree from the Department of Aerospace Engineering, Osaka Prefecture University, Osaka, Japan, in 2005, and the M.E. and Ph.D. degrees from the Division of Electrical, Electronic and Information Engineering, Osaka University, Osaka, in 2008 and 2011, respectively.

In 2011, he was a Post-Doctoral Researcher with Osaka University, and Colorado State University, Fort Collins, CO, USA, and also a Post-Doctoral Fellow of the Research Fellowship for Young Scientists sponsored by the Japan Society for the Promotion of Science. In 2012, he joined Japan Aerospace Exploration Agency, Tokyo, Japan, where he is an Associate Senior Researcher. He concurrently serves as a Visiting Associate Professor with Tokyo Metropolitan University, Tokyo. His research interests include weather radar remote sensing, radar-based analyses, and applications for general and aviation weather.

Tomoo Ushio (Life Fellow, IEEE) received the B.S., M.S., and Ph.D. degrees in electrical engineering from Osaka University, Osaka, Japan, in 1993, 1995, 1998, respectively.

He was with the Global Hydrology and Climate Center, Huntsville, AL, USA, as a Post-Doctorate Researcher from 1998 to 2000. In 2000, he joined the Department of Aerospace Engineering, Prefecture University, Osaka. In 2006, he was with the Department of Electrical, Electronic and Infocommunication Engineering, Osaka University, as an Associate Professor, where he is a Professor. His research specialties are radar-based remote sensing, passive and active remote sensing of the atmosphere from spaceborne platforms, and atmospheric electricity.

Hiroshi Kikuchi (Member, IEEE) received the B.S. degree from the Department of Engineering, Doshisha University, Kyoto, Japan, in 2008, and the M.S. and Ph.D. degrees from the Division of Electrical, Electronic and Information Engineering, Osaka University, Osaka, Japan, in 2010 and 2013, respectively.

He joined the Division of Electrical, Electric and Information Engineering, Osaka University, as a Specially Appointed Researcher, in 2013. In 2017, he was a Research Assistant Professor with Tokyo Metropolitan University, Tokyo, Japan. In 2018, he joined The University of Electro Communications, Chofu, Japan, where he is an Assistant Professor. His research specialties are remote sensing for atmospheric electricity with spaceborne platforms, and the weather radar remote sensing and the development of the radar system.